Inverse-designed growth-based cellular metamaterials

van 't Sant, S.; Thakolkaran, P.; Martínez, Jonàs; Kumar, Siddhant

DOI
10.1016/j.mechmat.2023.104668

Publication date
2023

Document Version
Final published version

Published in
Mechanics of Materials

Mechanics of Materials 182 (2023) 104668

Contents lists available at ScienceDirect

Mechanics of Materials

journal homepage: www.elsevier.com/locate/mecmat

Inverse-designed growth-based cellular metamaterials

Sikko Van 't Sant [a,1], Prakash Thakolkaran [a,1], Jonàs Martínez [b], Siddhant Kumar [a,*]

[a] Department of Materials Science and Engineering, Delft University of Technology, 2628 CD Delft, The Netherlands
[b] Université de Lorraine, CNRS, Inria, LORIA, F-54000, Nancy, France

ARTICLE INFO

Dataset link: https://github.com/mmc-group/inverse-designed-growth-based-metamaterials

Keywords:
Cellular metamaterials
Machine learning
Inverse Design
Growth process

ABSTRACT

Advancements in machine learning have sparked significant interest in designing mechanical metamaterials, i.e., materials that derive their properties from their inherent microstructure rather than just their constituent material. We propose a data-driven exploration of the design space of growth-based cellular metamaterials based on star-shaped distances. These two-dimensional metamaterials are based on periodically-repeating unit cells consisting of material and void patterns with non-trivial geometries. Machine learning models exploiting large datasets are then employed to inverse design growth-based metamaterials for tailored anisotropic stiffness. Firstly, a forward model is created to bypass the growth and homogenization process and accurately predict the mechanical properties given a finite set of design parameters. Secondly, an inverse model is used to invert the structure–property maps and enable the accurate prediction of designs for a given anisotropic stiffness query. We successfully demonstrate the frameworks' generalization capabilities by inverse designing for stiffness properties chosen from outside the domain of the design space.

1. Introduction

With the ever-improving manufacturing capabilities and computational power, mechanical metamaterials (Kadic et al., 2013) are pushing the boundaries of exhibiting exotic or tailored properties. What started with the search for auxetic behavior (negative Poisson's ratio) (Lakes, 1987; Hengsbach and Lantada, 2014; Grima and Evans, 2000; Imbalzano et al., 2016) has now led the way to designer metamaterials with high strength-to-weight ratio (Zheng et al., 2014; Meza et al., 2014), high energy absorption (Bauer et al., 2021; Wu et al., 2022), anisotropic stiffness tailoring (such as for patient-specific bone implants) (Kumar et al., 2020; Bastek et al., 2022; Zheng et al., 2021; Jiang et al., 2021; Amorim et al., 2019), mechanical cloaking (Wang et al., 2022), prescribed failure loads (Injeti et al., 2019) and more. Usually, these metamaterials are constructed by tessellating unit cells or lattices in a periodic fashion. While a lot of research has been dedicated to the design of mechanical metamaterials (often as networks of trusses, plates, and shells), most designs are fundamentally based on a few ad hoc unit cells identified over the years (e.g., by mimicking crystal lattices) and hardly follow any design convention. Lately, unit cells based on irregular patterns (Kumar et al., 2020; Liu et al., 2022; Martínez et al., 2019; Martínez, 2021) are attracting interest as they enable a much larger and seamless design and property space. Recently, Martínez et al. (2019) presented a unique design space of metamaterials using a growth algorithm governed by a star-shaped distance. It offers a continuous, high-dimensional, but compact design representation (as opposed to combinatorial design spaces (Panetta et al., 2015; Schumacher et al., 2015) which are computationally challenging) and a vast space of attainable effective mechanical properties such as tunable anisotropic stiffness and auxeticity. The method was further extended in Martínez (2021) to allow for varying thickness of the solid phase to expand the space of possible cellular geometries.

However, designing intricate unit cells for metamaterials is not a trivial task, as the designs are often described by highly unintuitive parameterization. Hence, before the introduction of machine learning (ML) to the mechanics of materials, metamaterial designs were often explored in a trial-and-error fashion, i.e., iteratively extracting the effective mechanical properties of several designs using forward simulations (e.g., numerical homogenization) until the target properties have been achieved. Each simulation is often computationally expensive, which can severely limit the exploration of the design space.[2] Data-driven and ML methods have increasingly overtaken this rather inefficient way of design optimization. Neural networks (NN) (LeCun et al., 2015) – a class of ML methods – can theoretically approximate any arbitrarily complex mapping, given a sufficient amount of training data (Cybenko, 1989). Leveraging modern computing hardware,

* Corresponding author.
E-mail address: Sid.Kumar@tudelft.nl (S. Kumar).

[1] Equal contributions.

[2] While topology optimization (Sigmund and Maute, 2013) has stepped up to the challenge of designing structures with tailored properties, the pixel-/voxel-based approach therein is not always applicable to metamaterials with complex design parameterizations.

https://doi.org/10.1016/j.mechmat.2023.104668
Received 28 January 2023; Received in revised form 24 April 2023; Accepted 26 April 2023
Available online 2 May 2023

NNs can serve as computationally efficient surrogates for expensive mechanics simulations (Kumar and Kochmann, 2022). These powerful capabilities have enabled orders of magnitude of acceleration for the design of, e.g., pixelated composites (Gu et al., 2018a,b; Yang et al., 2021; Wang et al., 2022, 2020), kirigami-based materials (Alderete et al., 2022; Hanakata et al., 2020; Liu et al., 2021), truss lattices in the two- (Wilt et al., 2020; He et al., 2022; Maurizi et al., 2022; Ma et al., 2020) and three-dimensional space (Bastek et al., 2022; Lee et al., 2022), spinodoid metamaterials (Kumar et al., 2020; Zheng et al., 2021), and triply-periodic minimal surface-based metamaterials (Meyer et al., 2022; Lu and Wang, 2022). The design process is often a combination of a NN (as a surrogate of the forward simulation) embedded inside a classical design optimization framework (Gu et al., 2018b; Kollmann et al., 2020; Shin et al., 2022; Lee et al., 2022). Note that finding an optimal metamaterial design is an ill-posed problem, as several designs may exhibit similar mechanical behavior. Consequently, the optimization-based methods are sensitive to the initial guess and require several runs to avoid producing suboptimal local minima. In contrast, the idea of using an NN-based inverse framework, i.e., directly mapping the properties back to the design parameters, has only recently gained attention. Kumar et al. (2020) and Bastek et al. (2022) proposed using a second NN to map the properties back to the structures while eliminating the ill-posedness of inverse design by using a custom loss function. Here, the need for an optimization process is bypassed, and designs are efficiently obtained given a property query. The inverse model can be viewed as an optimizer for all conceivable inverse problems by analyzing the entire property space via a dataset, enabling a comprehensive assessment of the property space and an effective and efficient solution across a wide range of design scenarios. We take inspiration from these works and develop a model for the inverse design of growth-based cellular metamaterials.

In the following, we present an ML framework for inverse designing cellular metamaterials given by a growth process parameterized with two different star-shaped sets. In Section 2, we introduce the geometry generation strategy, followed by the homogenization method used to extract its effective mechanical properties. Section 3 describes the machine learning-based inverse design framework. In Section 4, we deploy the trained models to inverse design for a range of different anisotropic stiffness queries, as well as for properties that stem from microstructures outside the design space of our growth-based cellular metamaterials. Finally, we conclude our findings in Section 5.

2. Growth-based cellular metamaterials

2.1. Growth-process based design space

We consider the discrete growth process algorithm presented by Martínez (2021) to generate the cellular materials. The algorithm outputs a two-dimensional image consisting of periodically tessellated unit cells with a solid and void phase distribution. We consider square-shaped unit cells of both size and resolution equal to $K \times K$ – each with a nucleus at its center. A star shape grows from the nucleus of all the unit cells simultaneously while obeying periodic boundary conditions. The process ceases whenever and wherever a growing shape centered around a nucleus comes into contact with that of another nucleus (see Fig. 1a).

The growth process is parameterized by two compact, non-convex, star-shaped sets: $\mathcal{S}, \mathcal{S}^* \subset \mathbb{R}^2$ centered around a nucleus $\boldsymbol{q} \in \mathcal{S}$. We call a set $\mathcal{S}$ star-shaped if, for any point $\boldsymbol{x} \in \mathcal{S}$, the line segment $[\boldsymbol{x}, \boldsymbol{q}]$ is contained in $\mathcal{S}$. $\mathcal{S}$ describes the initial shape around the nucleus when the growth process is started, while $\mathcal{S}^*$ determines the stopping criterion of the growth process (as described later). The boundary of the star-shaped set $\mathcal{S}$ can be represented in polar coordinates by a continuous function $\psi_{\mathcal{S}} : [0, 2\pi) \to [r_{\min}, r_{\max}]$, where $r_{\min} > 0$ and $r_{\max} \geq r_{\min}$ are the minimum and maximum Euclidean distance from the nucleus $\boldsymbol{q}$ to the set boundary, respectively. The boundary functions are parameterized by $n > 0$ known radial spans $\mathcal{R} = \{r_i : i = 1, \dots, n\}$ at equally spaced polar angles $\{\alpha_i = 2\pi(i-1)/n : i = 1, \dots, n\}$, such that $\psi_{\mathcal{S}}(\alpha_i) = r_i$ for all $i = 1, \dots, n$. Subsequently, the boundary function is constructed using a polar cubic interpolation method, ensuring that the function values lie between the minimum and maximum radial bounds. The boundary of $\mathcal{S}^*$ is analogously represented and parameterized by $\psi^*_{\mathcal{S}} : [0, 2\pi) \to [r^*_{\min}, r^*_{\max}]$, with the parameters distinguished by an additional superscript $(\cdot)^*$.

The growth process is governed by a star-shaped distance induced by $\mathcal{S}$. The distance between a point $\boldsymbol{x} \in \mathbb{R}^2$ and the associated nucleus $\boldsymbol{q}$ is defined as

$$d_{\mathcal{S}} = \frac{\|\boldsymbol{x} - \boldsymbol{q}\|}{\psi_{\mathcal{S}}(\angle(\boldsymbol{x} - \boldsymbol{q}))} \tag{1}$$

where $\angle : \mathbb{R}^2 \to [0, 2\pi)$ denotes the 2-argument arctangent function, i.e., atan2$(\cdot)$. Hence, the star-shaped distance $d_{\mathcal{S}}$ is equal to the factor by which the star-shaped set $\mathcal{S}$ (centered around q) has to be isotropically scaled to include the point x in the boundary $\psi_{\mathcal{S}}$. This distance is used to iteratively grow the star shape defined by $\mathcal{S}$ around the nucleus. The growth of a star shape ceases at a point $\boldsymbol{x}$, i.e., in the direction given by $\angle(\boldsymbol{x} - \boldsymbol{q})$, if a closed Euclidean disk $\mathcal{B}_r$ of radius $r = \mathcal{S}^*(\angle(\boldsymbol{x} - \boldsymbol{q}))$ and centered at $\boldsymbol{x}$ intersects any other simultaneously growing shape corresponding to another nucleus (see Fig. 1a). At the end of the growth process, the union of all fully grown star-shaped sets corresponds to the void phase. The remaining domain corresponds to the solid phase. A post-processing step is applied after the growth process to ensure that the solid phase forms a single connected periodic structure. For more details on the implementation, please refer to Martínez (2021) and the open-source code.[3]

The growth process – governed by $\mathcal{S}$ and $\mathcal{S}^*$ – is controlled by $2n$ parameters which are collectively denoted by $\boldsymbol{\Theta} = \{r_1, \dots, r_n, r^*_1 \dots, r^*_n\}$. We require a sufficiently large database of structure–property pairs to explore the mechanical design space of growth-based cellular metamaterials. To this end, we generate $N \gg 1$ designs by randomly sampling the radii $\{r_1, \dots, r_n\}$ and $\{r_1 *, \dots, r^*_n\}$ with uniform distribution from $[r_{\min}, r_{\max}]$ and $[r^*_{\min}, r^*_{\max}]$, respectively.

2.2. Homogenization of growth-based cellular metamaterials

For each cellular pattern (see Fig. 1b), we compute the effective mechanical stiffness via numerical homogenization of a representative volume element, i.e., the unit cell here. The solid phase is modeled as an isotropic and linearly elastic material with Young's modulus E_b and Poisson's ratio $\nu_b = 0.3$. For numerical stability, the void region is also modeled as an isotropic and linearly elastic material with small but non-zero Young's modulus $E_v = 10^{-6} E_b$ and Poisson's ratio $\nu_v = \nu_b$. Without the loss of generality, all stiffness values henceforth are normalized with respect to E_b and, therefore, eliminate the need for units.

The effective elastic response of the unit cell is represented by a fourth-order stiffness tensor $\mathbb{C}$. Note that here we assume plane strain conditions. The effective stiffness is computed by applying three different average strains $\langle \epsilon \rangle$ (two uniaxial compressions and one simple shear loading along the principal axes) with periodic boundary conditions to the unit cell and solving the linear system of equations $\langle \sigma_{ij} \rangle = \mathbb{C}_{ijkl} \langle \epsilon_{kl} \rangle$ (using Einstein's summation convention) for each case, where $\langle \boldsymbol{\sigma} \rangle$ denotes the volume-averaged stress in the unit cell obtained by satisfying static equilibrium. Using the major and minor symmetries, the stiffness tensor can also be rearranged into the Mandel notation as

$$\hat{\boldsymbol{C}} = \begin{bmatrix} \hat{C}_{11} & \hat{C}_{12} & \hat{C}_{13} \\ \hat{C}_{12} & \hat{C}_{22} & \hat{C}_{23} \\ \hat{C}_{13} & \hat{C}_{23} & \hat{C}_{33} \end{bmatrix} = \begin{bmatrix} \mathbb{C}_{1111} & \mathbb{C}_{1122} & \sqrt{2}\mathbb{C}_{1112} \\ \mathbb{C}_{1122} & \mathbb{C}_{2222} & \sqrt{2}\mathbb{C}_{2212} \\ \sqrt{2}\mathbb{C}_{1112} & \sqrt{2}\mathbb{C}_{2212} & 2\mathbb{C}_{1212} \end{bmatrix}, \tag{2}$$

[3] https://github.com/mfx-inria/auxeticgrowthprocess2d.

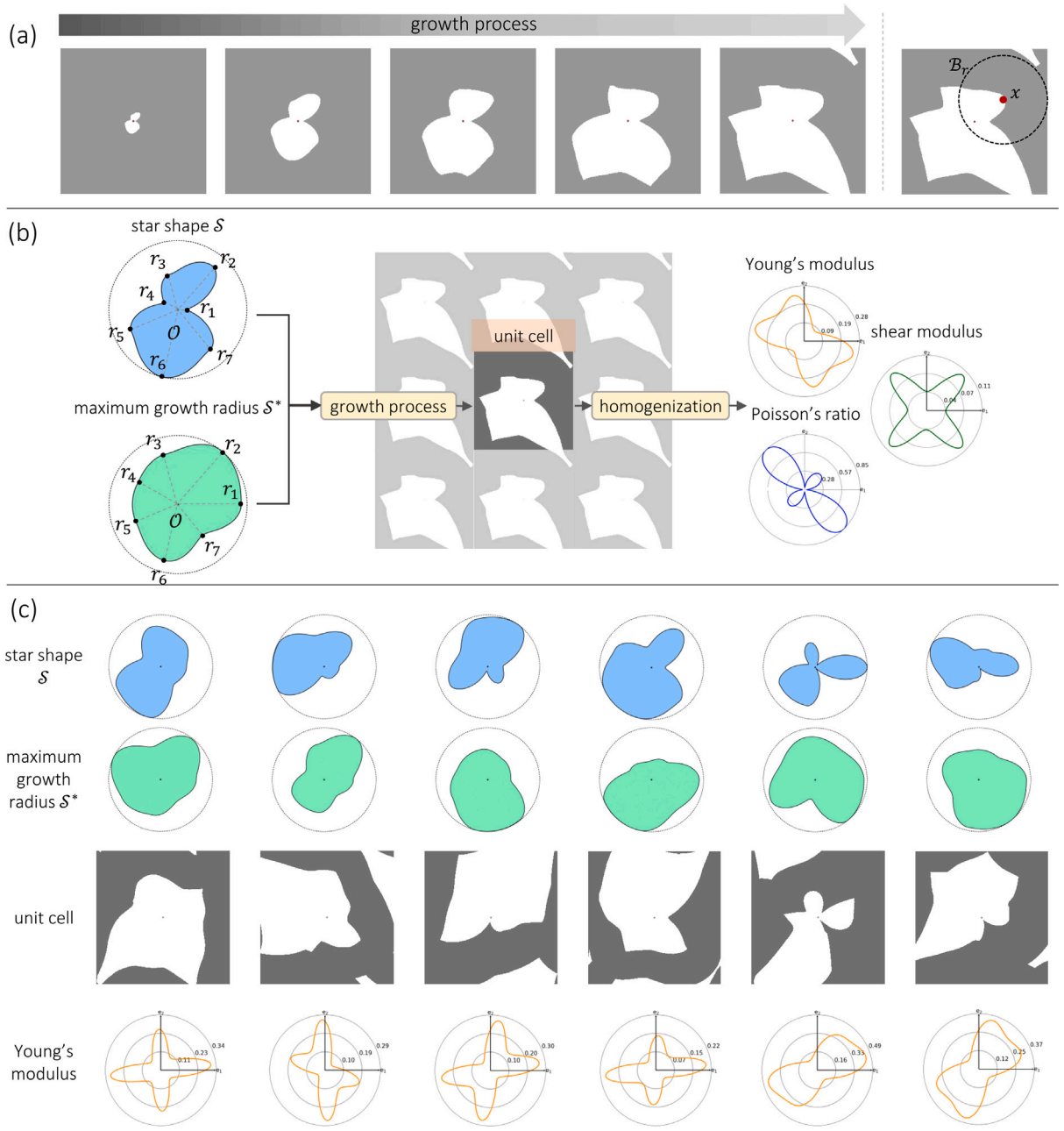

Fig. 1. (a): Illustration of the discrete growth process and its stopping criterion. (b): The growth algorithm requires a nucleating star-shape S and maximum growth radius S^* to create the microstructure. The final unit cell is constructed by solidifying the space not occupied by the resulting star shape and setting the rest as void. This periodic black-and-white image is then fed into an FFT-based homogenization framework (with periodic boundary conditions), and the effective stiffness tensor $\mathbb{C}$ (equivalently, $\hat{\boldsymbol{C}}$ or $\boldsymbol{\xi}$) is extracted. The directional properties, such as Young's modulus, shear modulus, and Poisson's ratio, are readily available from the stiffness tensor. Each point in the polar plots represents the effective property in the corresponding direction. (c): A selection of microstructures generated using diverse examples of S and S^*, and their corresponding directional Young's modulus.

where $\hat{\boldsymbol{C}}$ is a symmetric and positive-definite matrix. The independent components can be further reduced to

$$\boldsymbol{\xi} = (\hat{C}_{11}, \hat{C}_{12}, \hat{C}_{13}, \hat{C}_{22}, \hat{C}_{23}, \hat{C}_{33})^{\intercal}. \tag{3}$$

For the scope of this work, we use the Fast Fourier Transform (FFT) based homogenization algorithm developed by Brisard and Dormieux (2010).[4] Anisotropic elastic properties can be readily computed from $\mathbb{C}$ (equivalently, $\boldsymbol{\xi}$) as

$$\begin{aligned} E(\boldsymbol{d}) &= \left(\sum_{i,j,k,l}^{2} \mathbb{C}^{-1}_{ijkl} d_i d_j d_k d_l \right)^{-1}, \\ G(\boldsymbol{d}) &= \left(\sum_{i,j,k,l}^{2} 4 \cdot \mathbb{C}^{-1}_{ijkl} d_i n_j d_k n_l \right)^{-1}, \\ \nu(\boldsymbol{d}) &= -\left(\sum_{i,j,k,l}^{2} \mathbb{C}^{-1}_{ijkl} d_i d_j n_k n_l \right) E(\boldsymbol{d}), \end{aligned} \tag{4}$$

[4] https://sbrisard.github.io/janus/.

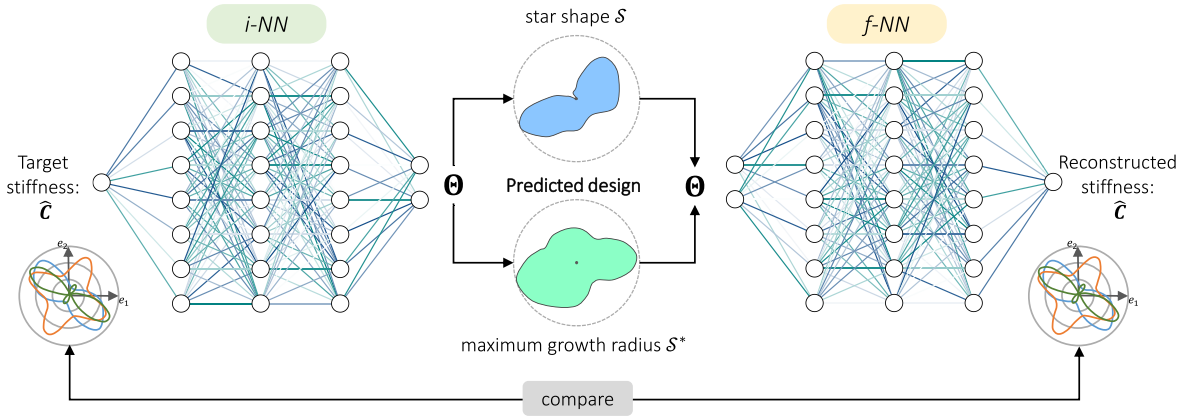

Fig. 2. The data-flow of training the inverse neural network is as follows. *(i)* A target stiffness $\hat{\boldsymbol{C}}$ (equivalently, $\boldsymbol{\xi}$) is passed into the inverse neural network (*i-NN*). *(ii)* The *i-NN* predicts the design parameters, i.e., the radial spans to construct the star shape $\mathcal{S}$ and maximum radial growth $\mathcal{S}^*$. *(iii)* The predicted design is passed into the pre-trained forward neural network (*f-NN*), which reconstructs the stiffness of the predicted design. *(iv)* The trainable parameters of *i-NN* are updated to minimize the difference between the target and reconstructed stiffness. The dual neural network strategy bypasses the ill-posedness of the inverse design challenge.

Table 1
List of parameters used for the growth process.

Parameter	Notation	Value
Resolution of microstructure image (pixels)	$K \times K$	128×128
Number of radial spans per star shape	n	7
Lower radial bound for star-shaped set $\mathcal{S}$	r_{min}	0.01
Upper radial bound for star-shaped set $\mathcal{S}$	r_{max}	1.0
Lower radial bound for star-shaped set $\mathcal{S}^*$	r^*_{min}	$0.2K$
Upper radial bound for star-shaped set $\mathcal{S}^*$	r^*_{max}	$0.6K$

where $E(\boldsymbol{d})$, $G(\boldsymbol{d})$, and $\nu(\boldsymbol{d})$ denote Young's modulus, shear modulus, and Poisson's ratio along any direction $\boldsymbol{d} \in S^1$, respectively. Here, $\boldsymbol{n}$ denotes the normal to the direction $\boldsymbol{d}$.

3. Data-driven inverse design

We create a large dataset $\mathcal{D} = \{\{\boldsymbol{\Theta}^{(i)}; \boldsymbol{\xi}^{(i)}\}, i = 1, \dots, N\}$ of N structure–property pairs with the aim to train a data-driven model for the inverse design of growth-based cellular metamaterials with tailored anisotropic mechanical stiffness. The inverse design framework is based on a combination of two neural networks (see Fig. 2 for a schematic).

A forward neural network (*f-NN*) takes as input the design parameters $\boldsymbol{\Theta}$ (i.e., the $2n$ radial spans for both the star shape and the maximum radial growth) and outputs the effective stiffness $\boldsymbol{\xi}$. The *f-NN* surrogates the entire process depicted in Fig. 1b – from creating the star-shapes and maximum growth shape using the radial spans to performing the growth process and extracting the stiffness of the resulting structure using numerical homogenization. Let $\mathcal{F}_\omega : \mathbb{R}^{2n} \to \mathbb{R}^6$ denote the *f-NN* with the trainable parameter set ω containing the weights and biases of the network. The stiffness predicted by the *f-NN* must be symmetric positive definite for physical admissibility. To ensure the same, we employ a Cholesky factorization transformation layer introduced by Jekel et al. (2022). Let $\boldsymbol{z} = (z_1, z_2, z_3, z_4, z_5, z_6)^\intercal$ be the output of $\mathcal{F}_\omega$. The stiffness prediction from the *f-NN* is then obtained as

$$\hat{\boldsymbol{C}} = \boldsymbol{L}\boldsymbol{L}^\intercal \qquad \text{with} \quad \boldsymbol{L} = \begin{bmatrix} \rho(z_1) & 0 & 0 \\ z_2 & \rho(z_3) & 0 \\ z_4 & z_5 & \rho(z_6) \end{bmatrix}, \tag{5}$$

where $\rho(\cdot) = \log\left(1 + \exp^{(\cdot)}\right)$ is the *softplus* activation function to ensure that the diagonal elements of $\boldsymbol{L}$ are positive. Since $\boldsymbol{L}$ is a lower triangular matrix with positive values on the diagonal, (5) represents a Cholesky factorization and $\hat{\boldsymbol{C}}$ is symmetric positive definite by construction. $\hat{\boldsymbol{C}}$ can be rearranged into $\boldsymbol{\xi}$ as per (3). The Cholesky factorization transformation from $\boldsymbol{z}$ to $\boldsymbol{\xi}$ is denoted by $\mathcal{H}$. The *f-NN* is trained by minimizing the stiffness prediction error across the dataset D as

$$\mathcal{F}_\omega \leftarrow \min_\omega \frac{1}{N} \sum_{i=1}^{N} \left\| \mathcal{H}\left[\mathcal{F}_\omega\left[\boldsymbol{\Theta}^{(i)}\right]\right] - \boldsymbol{\xi}^{(i)} \right\|^2, \tag{6}$$

Note that the forward problem is well-posed, as every design corresponds to a single, deterministic stiffness property.

After building the *f-NN*, we tackle the inverse challenge, i.e., predicting a set of design parameters based on a stiffness query. Let $\mathcal{V}_\tau : \mathbb{R}^6 \to \mathbb{R}^{2n}$ denote the inverse neural network (*i-NN*) with the trainable parameter set τ containing its weights and biases. The *i-NN* receives as input a target stiffness $\boldsymbol{\xi}$ and predicts the design parameters $\boldsymbol{\Theta} = \mathcal{V}_\tau[\boldsymbol{\xi}]$. However, unlike the training of *f-NN* in (6), training the *i-NN* is not straightforward. The inverse design problem is ill-posed, as multiple designs could correspond to a certain stiffness query. Therefore, training the *i-NN* based on minimizing the design prediction error, i.e., $\|\mathcal{V}_\tau[\boldsymbol{\xi}^{(i)}] - \boldsymbol{\Theta}^{(i)}\|^2$ directly, is not feasible. To circumvent this challenge, we follow the work of Kumar et al. (2020). We use the *f-NN* to reconstruct the stiffness of the predicted design from the *i-NN*. The reconstructed stiffness should match the target stiffness, irrespective of the predicted design parameters. This is formalized into the *i-NN* training by minimizing the error between the target and reconstructed stiffness across the dataset D, i.e.,

$$\mathcal{V}_\tau \leftarrow \min_\tau \frac{1}{N} \sum_{i=1}^{N} \left\| \mathcal{H}\left[\mathcal{F}_\omega\left[\mathcal{V}_\tau\left[\boldsymbol{\xi}^{(i)}\right]\right]\right] - \boldsymbol{\xi}^{(i)} \right\|^2 \tag{7}$$

Both neural networks are trained by backpropagation-based iterative minimization (Goodfellow et al., 2016) of the loss functions in (6) and (7). Note that the weights ω of the *f-NN* remain fixed and are not updated during the *i-NN* training. The *f-NN* serves as a computationally efficient and differentiable approximator of the map from design parameters to stiffness properties, which is required to perform backpropagation-based training of the *i-NN*.

4. Results

Table 1 summarizes the parameters used for growth process. Both *f-NN* and *i-NN* have the same architecture, a multilayer perceptron (Hornik et al., 1989) containing 5 hidden layers (not including the input and output layers) – each with 512 dimensions and softplus activation function (Nair and Hinton, 2010). A training set of $N = 800{,}000$ structure–property pairs is used for training. Note that the *f-NN* and *i-NN* are both trained on the same training set. Fig. 3 illustrates the diverse distribution and pairwise relationships for each stiffness component in the dataset. To ensure efficient training of the neural

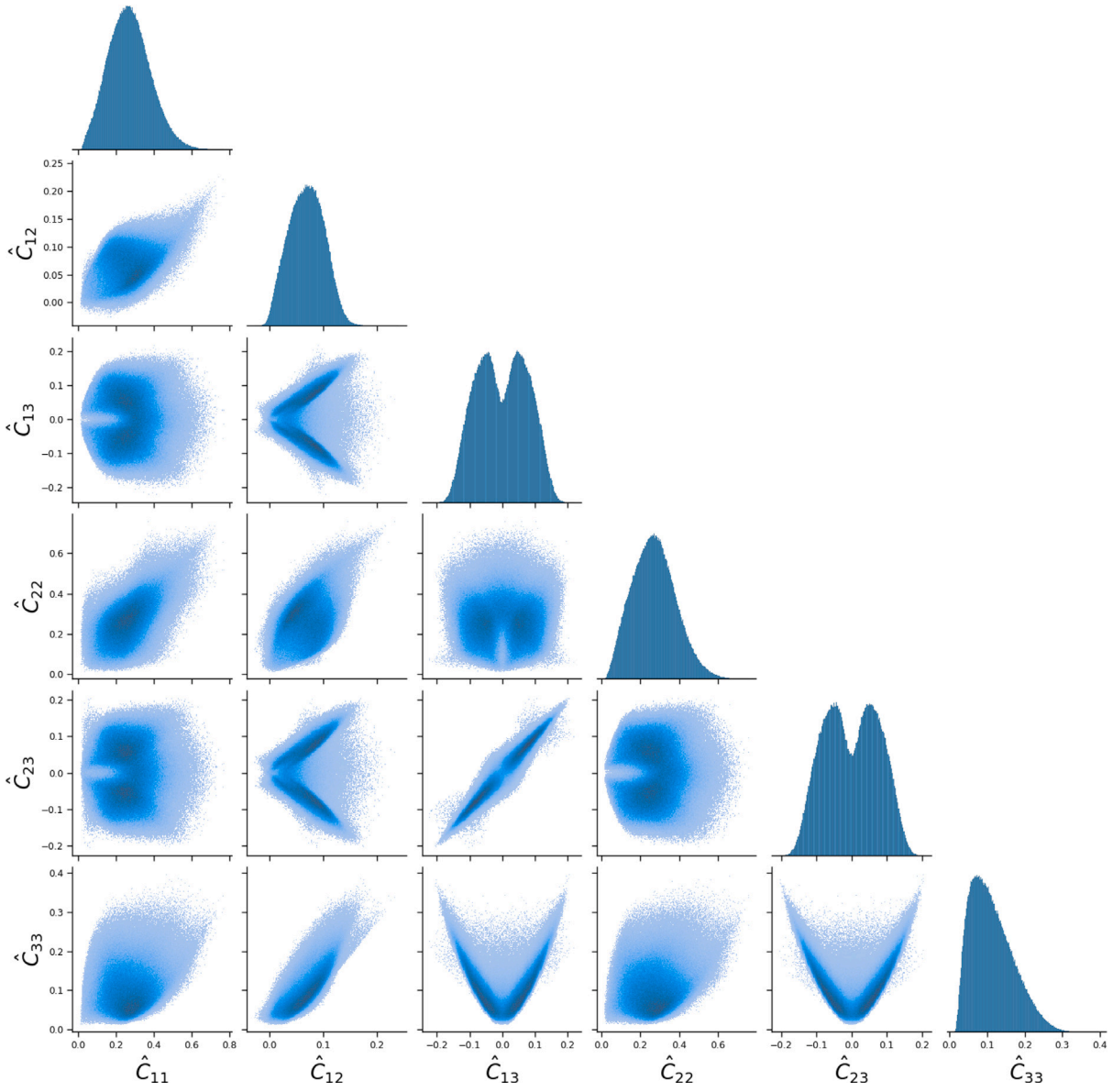

Fig. 3. Distribution and pairwise relationships for each stiffness component in the training dataset.

networks, all radial spans in any given $\boldsymbol{\Theta}$ are individually normalized to the range of $\{0, 1\}$ based on the minimum and maximum values across the training dataset. Both neural networks are trained using the optimizer Adam (Kingma and Ba, 2014) with a mini-batch size of 4096 and a learning rate of 0.001 for 1000 epochs. A separate validation set of 150,000 structure–property pairs is used to monitor the prediction accuracy and over-/underfitting during training. To avoid overfitting, an early stopping patience criterion is used, wherein the training is terminated if the validation loss (as defined in (6) and (7)) does not decrease within 50 epochs. Furthermore, we generate a test set of 50,000 structure–property pairs to evaluate the performance of the neural networks on data that is previously unseen during the training/validation. Additional implementation details and associated computational costs are presented in Appendix A.

Forward modeling accuracy: Fig. 4 summarizes the stiffness prediction accuracy of the *f-NN*. In a plot of true vs. predicted (from the *f-NN*) stiffness components, each data point from the test set should ideally lie on a line with unit slope and zero intercept. We obtain a goodness-of-fit (with respect to the ideal line) of $R^2 > 0.98$ for all the stiffness matrix components. Hence, with the *f-NN*, we get an accurate estimation of the stiffness properties given any randomly sampled S and S^*.

Inverse design accuracy: Fig. 5 summarizes the inverse design performance of the *i-NN*. Each stiffness in the test set is used as a target. The *i-NN* predicts a relevant design, whose stiffness is then reconstructed by the growth process and numerical homogenization. Note that the stiffness reconstruction during training is performed using the *f-NN*. However, during testing, numerical homogenization is used to avoid compounding any prediction error from the *f-NN*. Similar to the *f-NN*, the target and reconstructed stiffness should lie on the ideal line with unit slope and zero intercept, regardless of the differences between the original and predicted input parameters. We obtain $R^2 > 0.98$ for all the stiffness components for inverse design across the test set. In Fig. 6, for a selection of examples from the test set, the design parameters (i.e., the star shape S and maximum growth radius S^*) and geometry corresponding to the queried target stiffness are compared with that of the designs predicted by the *i-NN*. The significant difference in the design parameters and geometry despite a perfect match between their stiffness confirms the ill-posedness of the inverse design problem and verifies the need for the dual neural network approach. Note that some

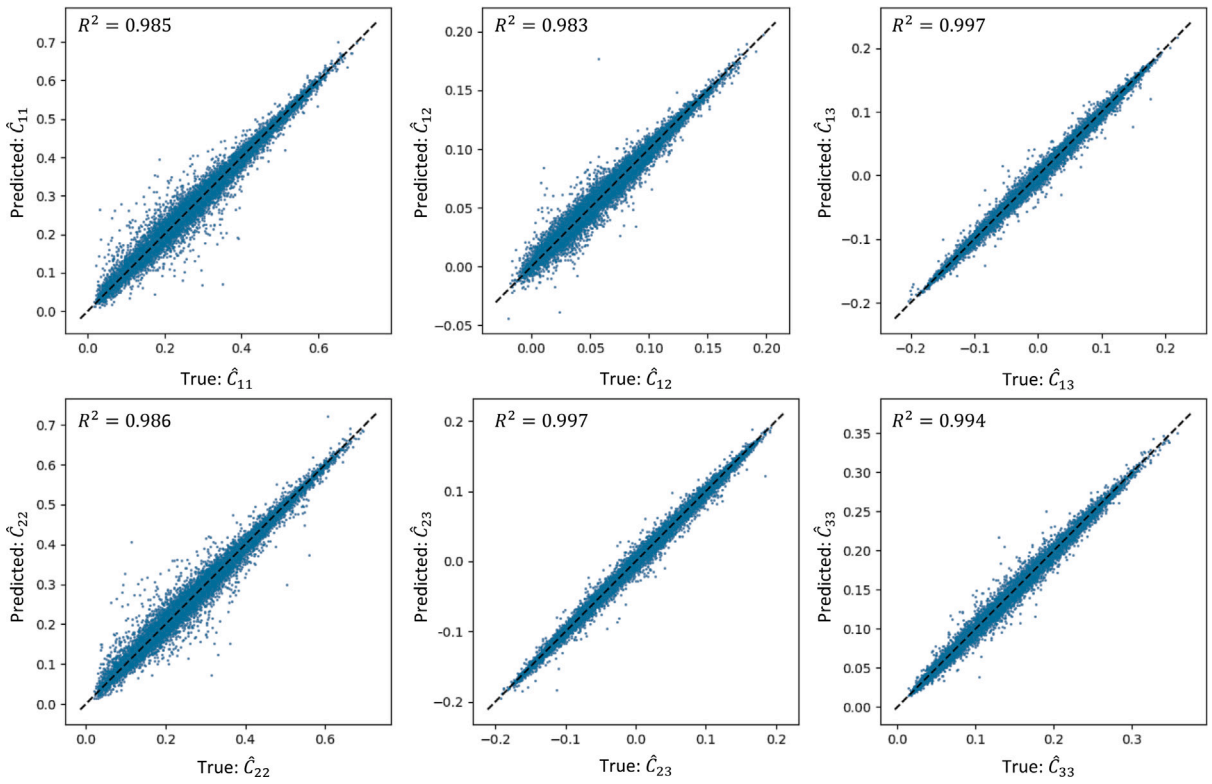

Fig. 4. True vs. predicted stiffness using the *f-NN* on the test set. All dashed lines represent the ideal line with unit slope and zero intercept; the corresponding R^2 goodness-of-fit are indicated.

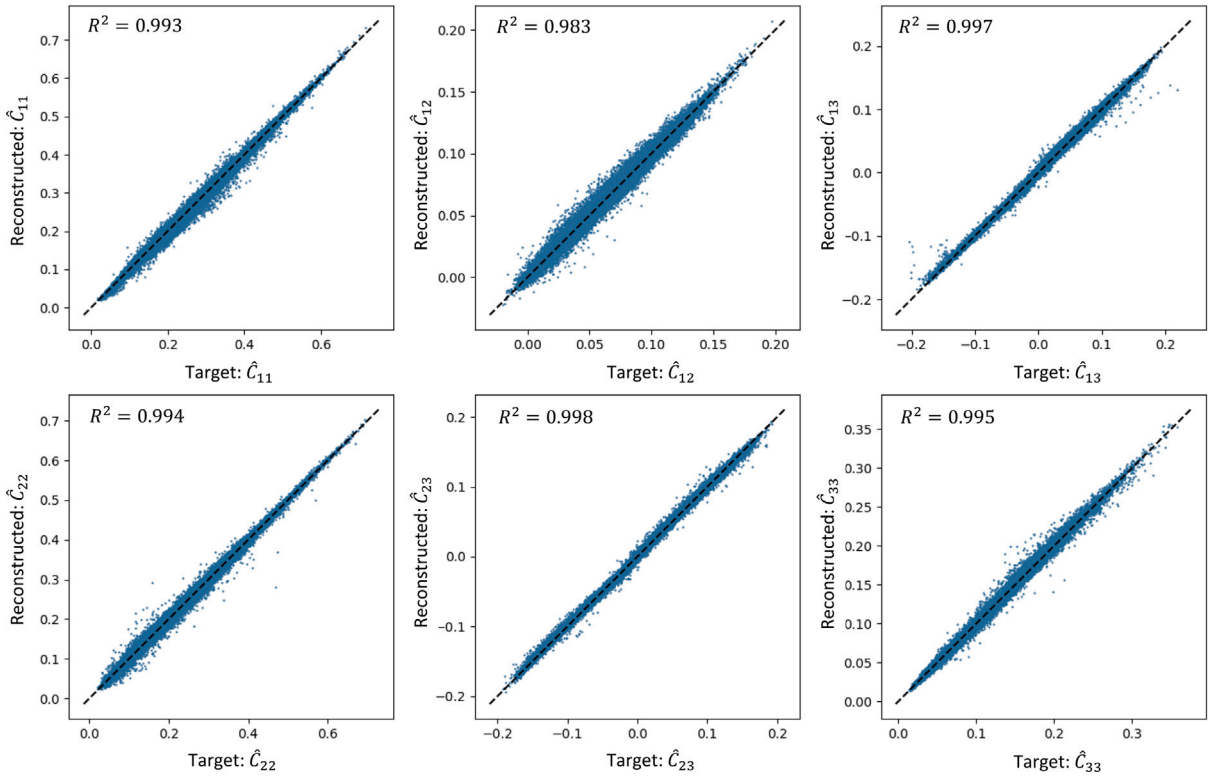

Fig. 5. Target vs. reconstructed stiffness of the design predictions from the *i-NN* on the test set. The stiffness reconstruction is performed via the growth process and numerical homogenization to avoid compounding errors (as opposed to stiffness reconstruction via the *f-NN* during training). All dashed lines represent the ideal line with unit slope and zero intercept; the corresponding R^2 goodness-of-fit are indicated.

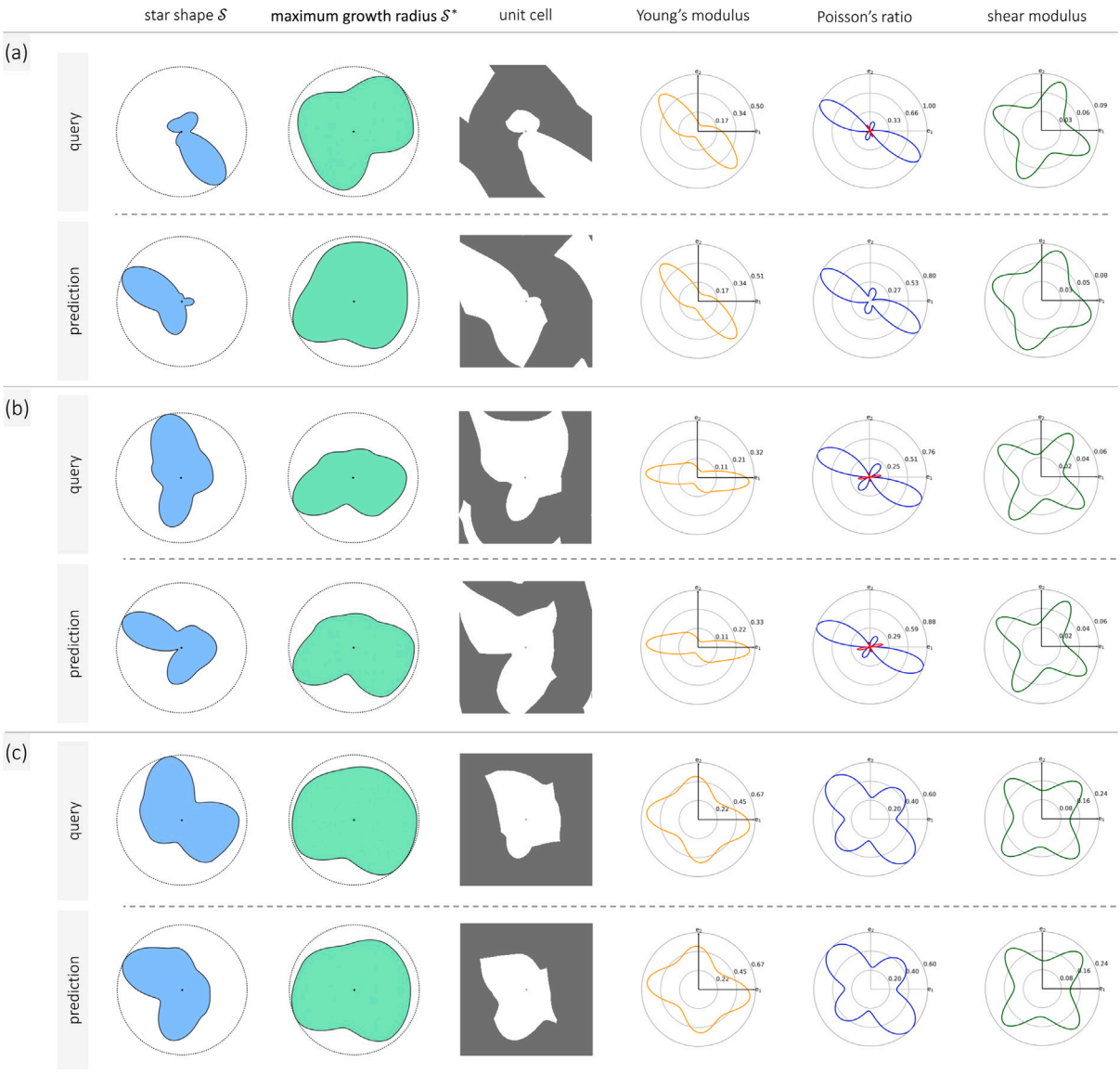

Fig. 6. (a)–(c): Selection of inverse design examples from the test set of growth-based cellular metamaterials. In each case, the *query* (top row) represents the design whose stiffness is used as target for inverse design. The *prediction* (bottom row) represents the design predicted by the *i-NN*. The corresponding plots of directional Young's modulus, Poisson's ratio, and shear modulus show good agreement despite significant difference in the query and predicted designs. This verifies the framework's ability to overcomes the ill-posedness of the inverse design challenge.

designs look visually similar, as the unit cell's geometry and material distribution are closely linked with its resulting anisotropic mechanical properties.

Moreover, generating large datasets can be a challenging and expensive task. To address this, we perform a data ablation study, the results of which are presented in Appendix B. We show that good forward modeling and inverse design accuracy can be achieved by training the neural networks using only 10% of the original dataset's design-stiffness pairs.

Inverse design generalizability: Instead of sampling the target stiffness from the property space of growth-based metamaterials itself, we test the generalizability of the *i-NN* by using as target the stiffness of arbitrary microstructures not achievable by the design space of choice here. The predicted designs and their properties — specifically, polar plots of directional Young's modulus, Poisson's ratio, and shear modulus (computed using (4)) are subsequently compared to those of the original designs in Fig. 7. A symmetric star-shape with eight spans, shown in Fig. 7a, cannot be perfectly replicated with seven prescribed spans in the chosen design space. The *i-NN* predicts a nearly square-shaped microstructure that closely matches the queried properties. The predictions have similar symmetry to the original query, albeit with a different topology. Fig. 7b considers a circular microstructure that would be challenging (although not impossible) to reproduce using the growth process since we prescribe an odd number of radial spans. The predicted microstructure is not visually similar to the original circle. However, the reconstructed stiffness components accurately match the target. The diagonal voids in the queried design of Fig. 7c are impossible for the growth process to replicate since it can only produce a single void per unit cell. Consequently, the predicted microstructure is significantly different from the original, yet it shows a similar void elongation orientation. Additionally, the stiffness properties of the predicted microstructure closely match those of the original.

Lastly, since we obtain both forward and inverse structure–property maps, the f-NN (which ensures the production of physically meaningful stiffness matrices via a Symmetric Positive Definite (SPD) layer) or FEM can be used to obtain a discrepancy between the target stiffness and the achieved stiffness. A high discrepancy indicates that either the target

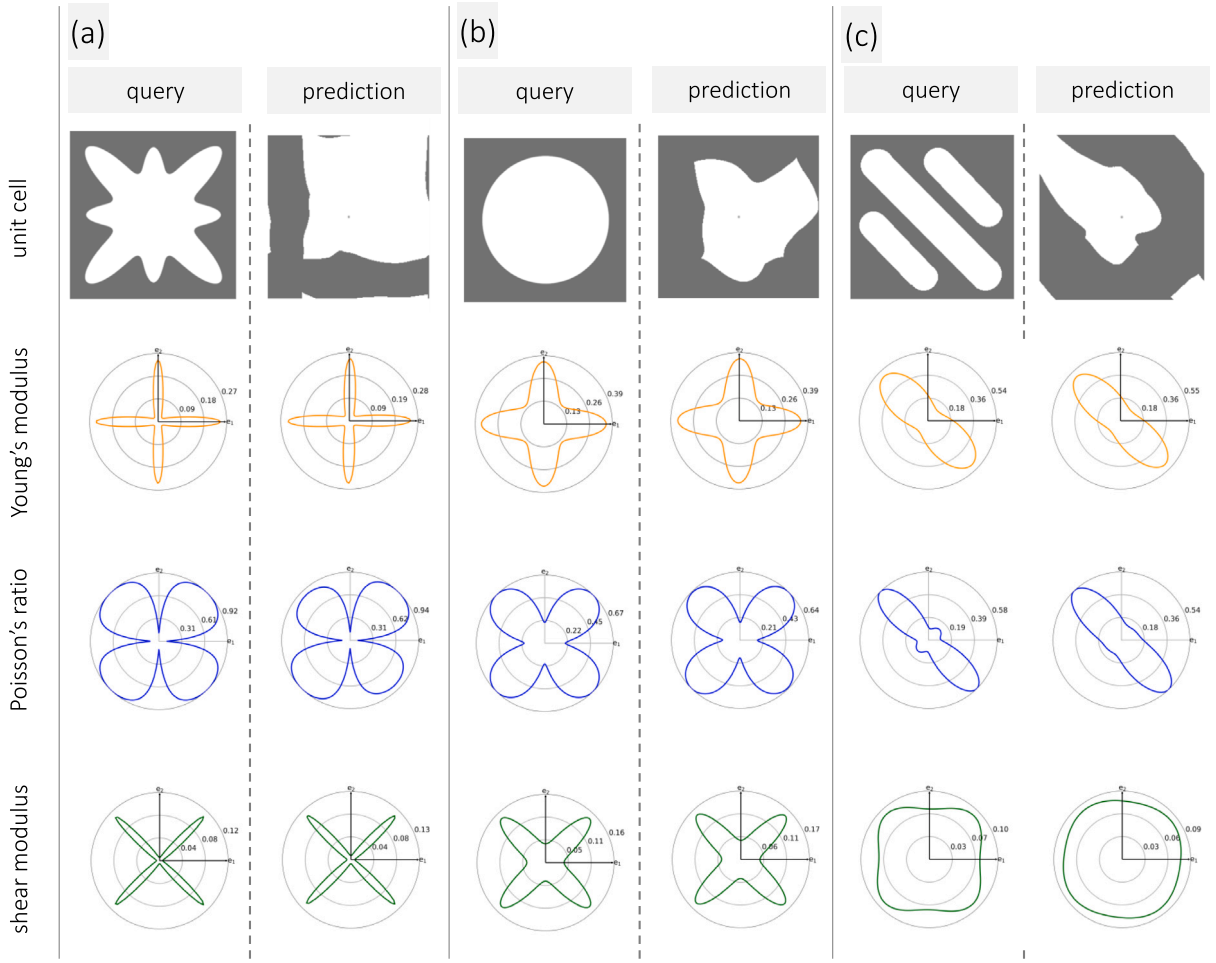

Fig. 7. (a)–(c): Selection of inverse design examples beyond the design space of growth-based cellular metamaterials. In each case, the *query* (left column) represents the design whose stiffness is used as target for inverse design. The designs are specifically chosen such that they cannot be reproduced by the current design space. The *prediction* (right column) represents the design predicted by the *i-NN*. The corresponding plots of directional Young's modulus, Poisson's ratio, and shear modulus show good agreement despite significant difference in the query and predicted designs. This exemplifies the framework's ability of accurately predicting growth-based cellular metamaterials given arbitrary stiffness targets.

stiffness is non-physical or outside the bounds of the property space spanned by the star-shaped metamaterials.

5. Conclusion and outlook

In this work, we developed a data-driven framework to instantly design two-dimensional metamaterials with tailored anisotropic elastic properties. The design space is based on the growth-based periodic cellular patterns introduced by Martínez (2021). The growth process is governed by two distinctive star-shaped sets (compactly parameterized by a small number of radial spans). The choice of the star-shaped sets defines the non-trivial geometry of the void inside each periodic unit cell. For the purpose of achieving targeted anisotropic elastic properties and bypassing the ill-posedness of the inverse design challenge, we developed a dual neural network approach. *(a)* A forward neural network predicts the independent components of the elastic stiffness matrix given the radial spans defining the star-shaped sets, and *(b)* an inverse neural network predicts the radial spans (corresponding to the star-shaped sets) given the components of the target stiffness matrix. We demonstrate that the forward neural network accurately predicts the mechanical properties given any arbitrary star-shape design; the inverse neural network accurately and efficiently reconstructs unit cell designs with elastic responses matching the target properties. Furthermore, we demonstrate that the inverse design framework can generalize to stiffness properties beyond those encompassed by the design space of growth-based metamaterials. While the proposed inverse design framework covers a large space of attainable anisotropic stiffness properties, future work may include: *(i)* the exploration of unit cells with multiple nuclei (with each corresponding to the same or different star-shaped sets) to enlarge the structure–property space, *(ii)* design for targeted mechanical response under finite deformations, *(iii)* ML methods such as generative adversarial (Goodfellow et al., 2016) or diffusion (Ho et al., 2020) networks to stochastically produce multiple dissimilar designs for a given target, and *(iv)* Bayesian neural networks (Goan and Fookes, 2020) account for data noise and uncertainties.

Declaration of competing interest

The authors declare that they have no known competing financial interests or personal relationships that could have appeared to influence the work reported in this paper.

Data and code availability

The data and codes generated in the current study are available at https://github.com/mmc-group/inverse-designed-growth-based-metamaterials.

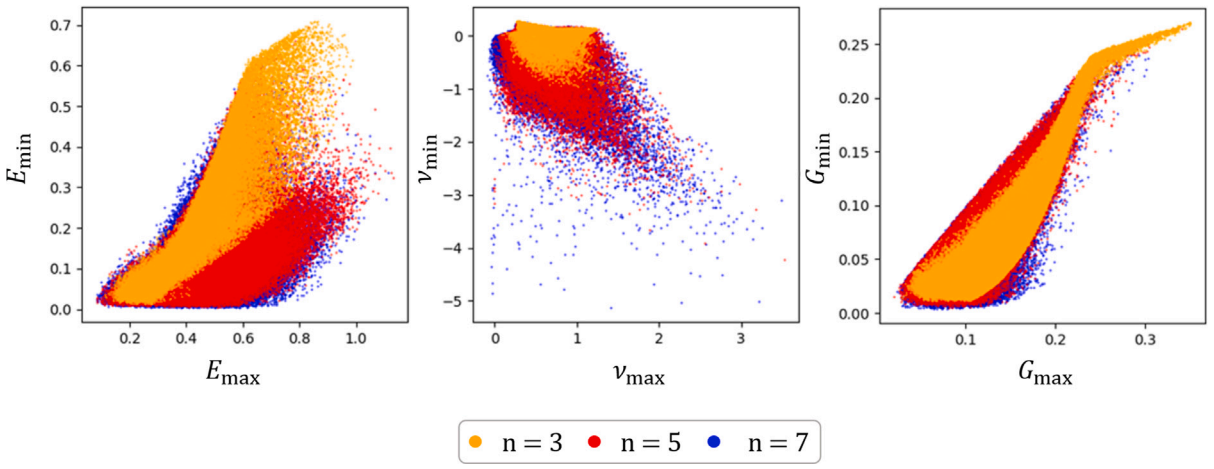

Fig. A.8. Scatter plot of the directional minimum and maximum of Young's modulus, shear modulus, and Poisson's ratio for a large number of star-shaped designs for different number of radial spans: $n = 3, 5, 7$. The coverage of the property spaces is assessed by investigating the spread of the data points in the scatter plot.

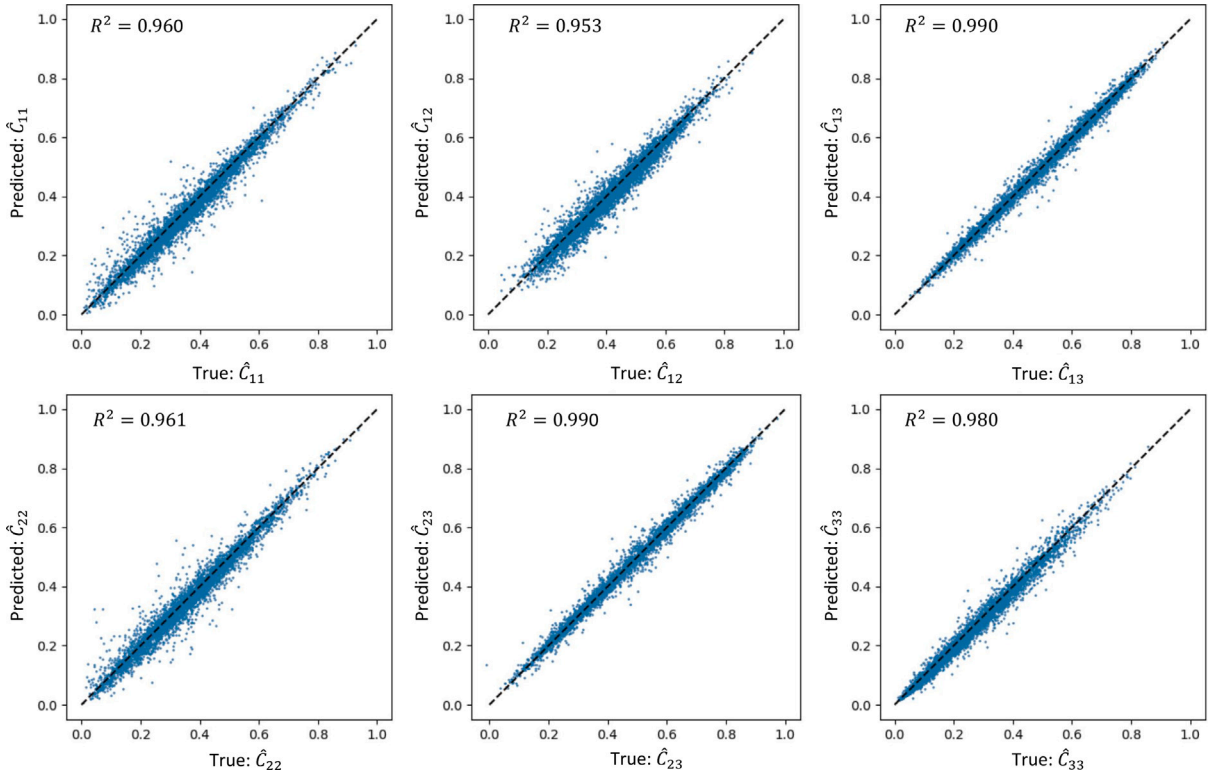

Fig. B.9. Target vs. reconstructed stiffness of the design predictions from the *f-NN* on the test set. **Here, the *f-NN* is trained on a dataset of the size of 10% of the original dataset size.** All dashed lines represent the ideal line with unit slope and zero intercept; the corresponding R^2 goodness-of-fit are indicated.

Appendix A. Additional implementation details

The workflow involved a dataset generation process consisting of growing the unit cell and the FFT-based homogenization for each star-shaped design, followed by sequential training of the *f-NN* and *i-NN* ML models on the training set of 800,000 samples. The dataset used in this study was generated on a computing cluster equipped with multiple Intel(R) Xeon(R) CPU E5-2670 v2 @ 2.50 GHz central processing units (CPU). The ML training was carried out on an Intel Xeon Gold 6248R with 24 cores and one NVIDIA RTX A5000 graphical processing unit. The computational time for each task is described in Table A.2.

Before generating the dataset, we investigated the design space for the growth-based cellular metamaterials by varying the number of spans (n) considered in the analysis. We tested three different options: n = 3, 5, and 7. The choice of n is based on balancing the expanse of the property space with the computational costs required since a higher number of spans would result in more complex parameters and would demand more data for accurate ML predictions. We generated

Table A.2
Computational times for individual tasks. Note that the runtimes reported are only rough estimates.

Task	Time
Growth process given a star-shaped design	12 ms
FFT-based homogenization of a unit cell	16 s
Training of the *f-NN* per epoch	13 s
Training of the *i-NN* per epoch	10 s
Total training of the *f-NN*	93 min
Total training of the *i-NN*	64 min
Inference of 1000 queries using *f-NN*	11 ms
Inference of 1000 queries using *i-NN*	8 ms

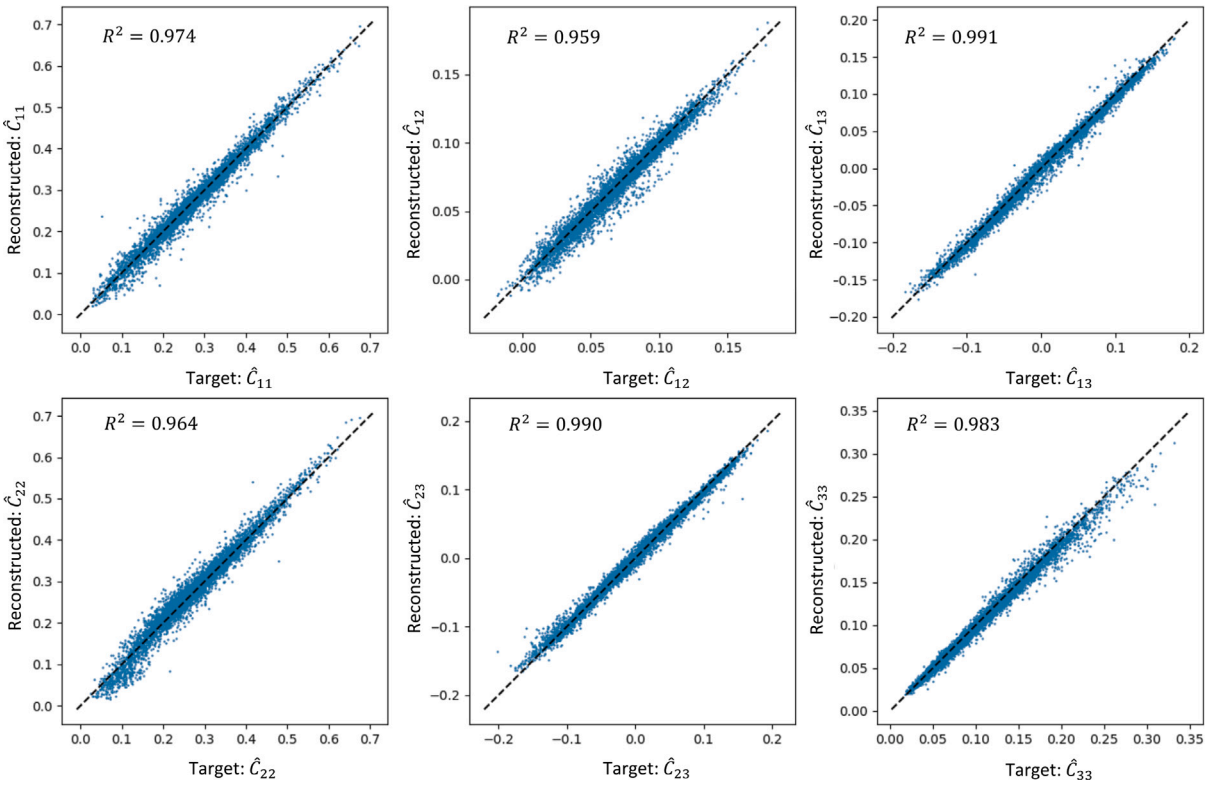

Fig. B.10. Target vs. reconstructed stiffness of the design predictions from the *i-NN* on the test set. **Here, the *i-NN* is trained on a dataset of the size of 10% of the original dataset size.** The stiffness reconstruction is performed via the growth process and numerical homogenization to avoid compounding errors (as opposed to stiffness reconstruction via the *f-NN* during training). All dashed lines represent the ideal line with unit slope and zero intercept; the corresponding R^2 goodness-of-fit are indicated.

scatter plots (see Fig. A.8) of the directional minimum and maximum of Young's modulus, shear modulus, and Poisson's ratio for a sufficiently large number of designs for each value of n. From the analysis of the scatter plots, we observe that the coverage of the property space expectedly increases as the number of spans increases from $n = 3$ to $n = 7$. However, the difference is only minimal between $n = 5$ and $n = 7$. Therefore, we selected $n = 7$ spans as a good trade-off between design complexity and computational costs.

Appendix B. Data ablation test

The computational expense of generating a large dataset can be mitigated by using a smaller dataset if the decrease in accuracy is minimal/acceptable. To this end, we re-train our neural networks using only 10% of the design-stiffness pairs from the original dataset. Hence, the resulting dataset sizes are 80,000, 15,000, and 5000 samples for the training set, validation set, and testing set, respectively. The corresponding forward and inverse prediction performances are presented in Figs. B.9 and B.10. As expected, the models trained on the reduced dataset showed slightly inferior performance compared to those trained on the larger dataset. However, the R^2 values indicate that the accuracy degradation is not significant. Thus, we conclude that our framework can still achieve comparable performance even when provided with a fraction of the original dataset, which is particularly useful in cases where data generation is a bottleneck.

References

Alderete, N.A., Pathak, N., Espinosa, H.D., 2022. Machine learning assisted design of shape-programmable 3D kirigami metamaterials. Npj Comput. Mater. 8 (1), 1–12.

Amorim, D.J.N., Nachtigall, T., Alonso, M.B., 2019. Exploring mechanical meta-material structures through personalised shoe sole design. In: Proceedings of the ACM Symposium on Computational Fabrication. pp. 1–8.

Bastek, J.-H., Kumar, S., Telgen, B., Glaesener, R.N., Kochmann, D.M., 2022. Inverting the structure–property map of truss metamaterials by deep learning. Proc. Natl. Acad. Sci. 119 (1), e2111505119.

Bauer, J., Kraus, J.A., Crook, C., Rimoli, J.J., Valdevit, L., 2021. Tensegrity metamaterials: Toward failure-resistant engineering systems through delocalized deformation. Adv. Mater. 33 (10), 2005647.

Brisard, S., Dormieux, L., 2010. FFT-based methods for the mechanics of composites: A general variational framework. Comput. Mater. Sci. 49 (3), 663–671.

Cybenko, G., 1989. Approximation by superpositions of a sigmoidal function. Math. Control Signals Systems 2 (4), 303–314.

Goan, E., Fookes, C., 2020. Bayesian neural networks: An introduction and survey. In: Case Studies in Applied Bayesian Data Science. Springer International Publishing, pp. 45–87. http://dx.doi.org/10.1007/978-3-030-42553-1_3.

Goodfellow, I., Bengio, Y., Courville, A., 2016. Deep Learning. MIT Press, http://www.deeplearningbook.org.

Grima, J., Evans, K., 2000. Auxetic behavior from rotating squares. J. Mater. Sci. Lett. 17 (19), 1563–1565.

Gu, G.X., Chen, C.-T., Buehler, M.J., 2018a. De novo composite design based on machine learning algorithm. Extreme Mech. Lett. 18, 19–28.

Gu, G.X., Chen, C.-T., Richmond, D.J., Buehler, M.J., 2018b. Bioinspired hierarchical composite design using machine learning: simulation, additive manufacturing, and experiment. Mater. Horiz. 5 (5), 939–945.

Hanakata, P.Z., Cubuk, E.D., Campbell, D.K., Park, H.S., 2020. Forward and inverse design of kirigami via supervised autoencoder. Phys. Rev. Res. 2 (4), 042006.

He, J., Kushwaha, S., Abueidda, D., Jasiuk, I., 2022. Exploring the structure-property relations of thin-walled, 2D extruded lattices using neural networks. arXiv preprint arXiv:2205.06761.

Hengsbach, S., Lantada, A.D., 2014. Direct laser writing of auxetic structures: present capabilities and challenges. Smart Mater. Struct. 23 (8), 085033.

Ho, J., Jain, A., Abbeel, P., 2020. Denoising diffusion probabilistic models. http://dx.doi.org/10.48550/ARXIV.2006.11239, URL: https://arxiv.org/abs/2006.11239.

Hornik, K., Stinchcombe, M., White, H., 1989. Multilayer feedforward networks are universal approximators. Neural Netw. 2 (5), 359–366.

Imbalzano, G., Tran, P., Ngo, T.D., Lee, P.V., 2016. A numerical study of auxetic composite panels under blast loadings. Compos. Struct. 135, 339–352.

Injeti, S.S., Daraio, C., Bhattacharya, K., 2019. Metamaterials with engineered failure load and stiffness. Proc. Natl. Acad. Sci. 116 (48), 23960–23965.

Jekel, C.F., Swartz, K.E., White, D.A., Tortorelli, D.A., Watts, S.E., 2022. Neural network layers for prediction of positive definite elastic stiffness tensors. arXiv preprint arXiv:2203.13938.

Jiang, W., Liao, W., Liu, T., Shi, X., Wang, C., Qi, J., Chen, Y., Wang, Z., Zhang, C., 2021. A voxel-based method of multiscale mechanical property optimization for the design of graded TPMS structures. Mater. Des. 204, 109655.

Kadic, M., Bückmann, T., Schittny, R., Wegener, M., 2013. Metamaterials beyond electromagnetism. Rep. Progr. Phys. 76 (12), 126501.

Kingma, D.P., Ba, J., 2014. Adam: A method for stochastic optimization. arXiv preprint arXiv:1412.6980.

Kollmann, H.T., Abueidda, D.W., Koric, S., Guleryuz, E., Sobh, N.A., 2020. Deep learning for topology optimization of 2D metamaterials. Mater. Des. 196, 109098.

Kumar, S., Kochmann, D.M., 2022. What machine learning can do for computational solid mechanics. In: Current Trends and Open Problems in Computational Mechanics. Springer, pp. 275–285.

Kumar, S., Tan, S., Zheng, L., Kochmann, D.M., 2020. Inverse-designed spinodoid metamaterials. Npj Comput. Mater. 6 (1), 1–10.

Lakes, R., 1987. Foam structures with a negative Poisson's ratio. Science 235 (4792), 1038–1040.

LeCun, Y., Bengio, Y., Hinton, G., 2015. Deep learning. Nature 521 (7553), 436–444.

Lee, S., Zhang, Z., Gu, G.X., 2022. Generative machine learning algorithm for lattice structures with superior mechanical properties. Mater. Horiz. 9 (3), 952–960.

Liu, K., Sun, R., Daraio, C., 2022. Growth rules for irregular architected materials with programmable properties. Science 377 (6609), 975–981.

Liu, T., Sun, S., Liu, H., An, N., Zhou, J., 2021. A predictive deep-learning approach for homogenization of auxetic kirigami metamaterials with randomly oriented cuts. Modern Phys. Lett. B 35 (01), 2150033.

Lu, Y., Wang, Y., 2022. Structural optimization of metamaterials based on periodic surface modeling. Comput. Methods Appl. Mech. Engrg. 395, 115057.

Ma, C., Zhang, Z., Luce, B., Pusateri, S., Xie, B., Rafiei, M.H., Hu, N., 2020. Accelerated design and characterization of non-uniform cellular materials via a machine-learning based framework. Npj Comput. Mater. 6 (1), 1–8.

Martínez, J., 2021. Random auxetic porous materials from parametric growth processes. Comput. Aided Des. 139, 103069.

Martínez, J., Skouras, M., Schumacher, C., Hornus, S., Lefebvre, S., Thomaszewski, B., 2019. Star-shaped metrics for mechanical metamaterial design. ACM Trans. Graph. 38 (4), 1–13.

Maurizi, M., Gao, C., Berto, F., 2022. Inverse design of truss lattice materials with superior buckling resistance. Npj Comput. Mater. 8 (1), 1–12.

Meyer, P.P., Bonatti, C., Tancogne-Dejean, T., Mohr, D., 2022. Graph-based metamaterials: Deep learning of structure-property relations. Mater. Des. 223, 111175.

Meza, L.R., Das, S., Greer, J.R., 2014. Strong, lightweight, and recoverable three-dimensional ceramic nanolattices. Science 345 (6202), 1322–1326.

Nair, V., Hinton, G.E., 2010. Rectified linear units improve restricted boltzmann machines. In: Proceedings of the 27th International Conference on Machine Learning (ICML-10). pp. 807–814.

Panetta, J., Zhou, Q., Malomo, L., Pietroni, N., Cignoni, P., Zorin, D., 2015. Elastic textures for additive fabrication. ACM Trans. Graph. 34 (4), 1–12.

Schumacher, C., Bickel, B., Rys, J., Marschner, S., Daraio, C., Gross, M., 2015. Microstructures to control elasticity in 3D printing. ACM Trans. Graph. 34 (4), 1–13. http://dx.doi.org/10.1145/2766926.

Shin, D., Cupertino, A., de Jong, M.H., Steeneken, P.G., Bessa, M.A., Norte, R.A., 2022. Spiderweb nanomechanical resonators via bayesian optimization: inspired by nature and guided by machine learning. Adv. Mater. 34 (3), 2106248.

Sigmund, O., Maute, K., 2013. Topology optimization approaches. Struct. Multidiscip. Optim. 48 (6), 1031–1055. http://dx.doi.org/10.1007/s00158-013-0978-6.

Wang, L., Boddapati, J., Liu, K., Zhu, P., Daraio, C., Chen, W., 2022. Mechanical cloak via data-driven aperiodic metamaterial design. Proc. Natl. Acad. Sci. 119 (13), e2122185119.

Wang, L., Chan, Y.-C., Ahmed, F., Liu, Z., Zhu, P., Chen, W., 2020. Deep generative modeling for mechanistic-based learning and design of metamaterial systems. Comput. Methods Appl. Mech. Engrg. 372, 113377.

Wilt, J.K., Yang, C., Gu, G.X., 2020. Accelerating auxetic metamaterial design with deep learning. Adv. Eng. Mater. 22 (5), 1901266.

Wu, W., Kim, S., Ramazani, A., Cho, Y.T., 2022. Twin mechanical metamaterials inspired by nano-twin metals: Experimental investigations. Compos. Struct. 291, 115580.

Yang, Z., Yu, C.-H., Buehler, M.J., 2021. Deep learning model to predict complex stress and strain fields in hierarchical composites. Sci. Adv. 7 (15), eabd7416.

Zheng, L., Kumar, S., Kochmann, D.M., 2021. Data-driven topology optimization of spinodoid metamaterials with seamlessly tunable anisotropy. Comput. Methods Appl. Mech. Engrg. 383, 113894.

Zheng, X., Lee, H., Weisgraber, T.H., Shusteff, M., DeOtte, J., Duoss, E.B., Kuntz, J.D., Biener, M.M., Ge, Q., Jackson, J.A., et al., 2014. Ultralight, ultrastiff mechanical metamaterials. Science 344 (6190), 1373–1377.